

Dissecting the Homunculus Nebula Around Eta Carinae With Spatially Resolved Near-Infrared Spectroscopy

Nathan Smith^{*†}

Center for Astrophysics and Space Astronomy, University of Colorado, 389 UCB, Boulder, CO 80309, USA

Accepted 2002 August 11. Received 2002 August 5; in original form 2002 July 10

ABSTRACT

Near-infrared emission lines provide unique diagnostics of the geometry, structure, kinematics, and excitation of η Carinae’s circumstellar ejecta, and give clues to the nature of its wind. The infrared spectrum is a strong function of position in η Car’s nebula, with a mix of intrinsic and reflected emission. Molecular hydrogen traces cool gas and dust in the polar lobes, while [Fe II] blankets their inner surfaces. These lines reveal the back wall of the SE polar lobe for the first time, and give the clearest picture yet of the 3-D geometry. Additionally, collisionally-excited [Fe II] reveals the kinematic structure of a recently discovered ‘Little Homunculus’ expanding inside the larger one. Equatorial gas in the ‘Fan’, on the other hand, shows a spectrum indicating recombination and fluorescent Ly α pumping. Some equatorial ejecta glow in the He I λ 10830 line, showing evidence for material ejected in the 1890 outburst of η Car. Closer to the star, the compact ‘Weigelt blobs’ are marginally resolved, allowing their infrared spectrum to be separated from the star for the first time. In general, infrared spectra reveal a coherent, directional dependence of excitation in the Homunculus: polar ejecta are collisionally excited, whereas equatorial ejecta are dominated by fluorescence and normal photoexcitation. These are important clues to the geometry of the central star’s UV radiation field. Reflected near-infrared emission lines also reveal interesting latitudinal dependence in the stellar wind.

Key words: circumstellar matter — reflection nebulae — stars: individual (η Carinae) — stars: mass loss — stars: winds, outflows

1 INTRODUCTION

The idiosyncratic massive star η Carinae and its bipolar Homunculus Nebula provide spectacular examples of a dense stellar wind and processed ejecta atop the HR Diagram. Its proximity and brightness allow detailed multiwavelength study, offering insight to the limits nature imposes on the stability of stars. η Car exhibits extreme spatial, temporal, and spectral complexity throughout the electromagnetic spectrum; infrared (IR) wavelengths afford us no exception, but they provide unique diagnostics of the wind and ejecta.

The shape, orientation, kinematics, and excitation of the Homunculus offer the best ways to investigate ejection physics of the Great Eruption, since most material was ejected in the 1840’s (Morse et al. 2001; Smith & Gehrz

1998; Currie et al. 1996). The Homunculus is a dusty nebula dominated by reflected starlight at optical wavelengths. This makes it problematic to study the kinematics and excitation of the Homunculus itself, because narrow emission lines originating in the polar lobes overlap with reflected emission (e.g., Hillier & Allen 1992; Davidson et al. 2001). IR wavelengths offer a way to mitigate this, with strong emission from the polar lobes in a few transitions of H₂ and [Fe II] (Smith & Davidson 2001). Furthermore, lower extinction in the IR allows us to peer *inside* the Homunculus to study embedded emission structures.

Spatially resolved long-slit spectroscopy allows us to view the reflected stellar spectrum from multiple directions. Most previous investigations of η Car’s IR spectrum have integrated light from the entire Homunculus (Whitelock et al. 1983; Allen, Jones, & Hyland 1985; McGregor, Hyland, & Hillier 1988) or the bright unresolved core (Hamann et al. 1994). Hamann et al. presented the optical to far-red spectrum observed in the SE lobe, revealing a reflected broad-line spectrum of the central star. Long-slit spectra presented here provide multiple viewing angles to η Car

* Email: nathans@casa.colorado.edu

† Visiting Astronomer, Cerro Tololo Inter-American Observatory, National Optical Astronomy Observatories, operated by the Association of Universities for Research in Astronomy, Inc., under cooperative agreement with the National Science Foundation.

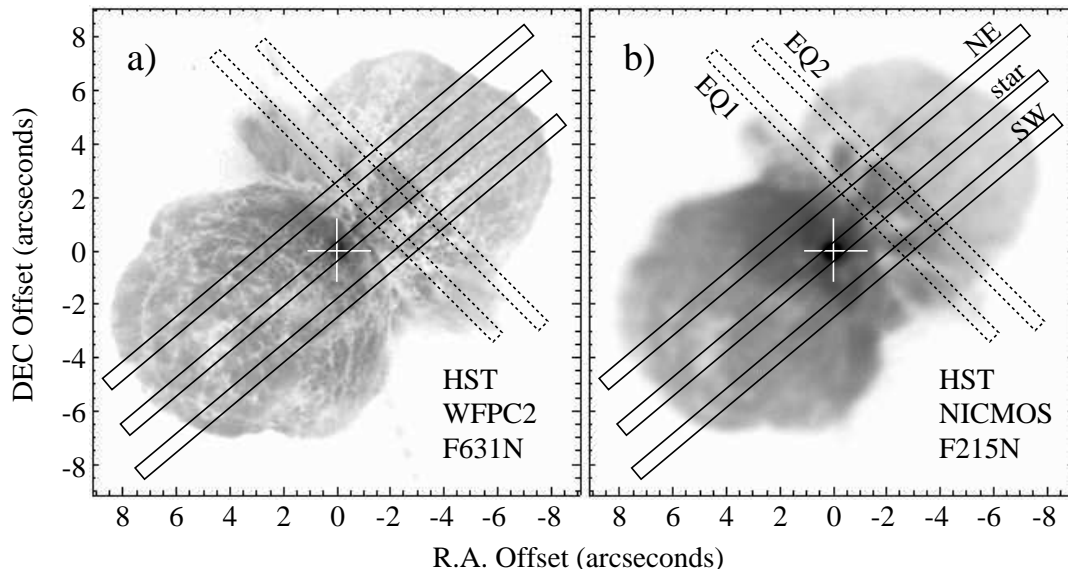


Figure 1. (a) A red *HST*/WFPC2 image of η Car (see Morse et al. 1998) showing orientations of OSIRIS apertures. (b) same as a but with a $\sim 2 \mu\text{m}$ continuum *HST*/NICMOS image from Smith & Gehrz (2000). Dotted boxes show positions of long-slit apertures crossing equatorial ejecta, discussed in §5. Slit positions are labeled with designations referred to in the text.

for the first time at wavelengths longer than $1 \mu\text{m}$. η Car was observed in March 2001, during its high-excitation state between “spectroscopic events” that repeat every 5.5 years (Damineli 1996). Latitudinal structure of the wind changes dramatically during this cycle (Smith et al. 2003), so these IR spectra also provide a benchmark for future spectroscopy.

New observations obtained at CTIO are presented in §2. Intrinsic IR emission lines are used to derive the structure of the Homunculus in §3, and in §4 and §5 other novel aspects of the IR spectra are presented. Finally, the central star, nearby ejecta, and reflected spectra are discussed in §6.

2 OBSERVATIONS

Long-slit spectra of η Carinae from 1 to $2.3 \mu\text{m}$ were obtained on 2001 March 13 and 14 using OSIRIS¹ mounted on the CTIO 4m telescope. Data were obtained in high-resolution mode, with an effective 2-pixel spectral resolution of about 100 km s^{-1} ($R \sim 3000$). These spectra are similar to observations obtained a year earlier in March 2000, for which preliminary results have already been presented (Smith 2001; Smith & Davidson 2001). However, the new data obtained in March 2001 are superior for several reasons, including better seeing ($\sim 0''.4$), and the alignment of the long slit aperture with the polar axis of the Homunculus at P.A. $= -50^\circ$ (see Figure 1). Spectra were obtained with the $\sim 0''.5$ -wide slit aperture centered on the central star, as well as two positions offset $\sim 1''$ to the NE and SW. A few spectra were also obtained with the slit oriented perpendicular to the polar axis of the Homunculus (labeled as ‘EQ1’ and ‘EQ2’ in Figure 1). Sky-subtraction was performed by chopping along the slit with offsets greater than the size of

the Homunculus. Wavelengths were calibrated using observations of an internal emission lamp. Flux calibration and telluric absorption correction were accomplished with reference to spectroscopic standard stars.

Figure 2 shows long-slit spectra of the Homunculus in the I, J, H, and K bandpasses observable from the ground, with long-slit spectra centered on the star and $1''$ NE (long-slit spectra for positions $1''$ SW are similar). NE positions show fainter emission features. It is clear from Figure 2 that the observed spectrum varies with position along the slit. There are essentially two different types of emission features present: 1) narrow emission lines emitted by gas in the Homunculus, and 2) broad emission lines in the wind of the central star reflected toward us by dust. The $\sim 0''.4$ seeing for these observations reveals complex spatial structure along the slit length, useful for future comparison with *HST*/STIS data. Various details concerning the spatial variation of these two types of features are discussed below.

3 SHAPE AND STRUCTURE OF EMISSION FROM THE POLAR LOBES

Proper motions for expanding debris in the Homunculus have been measured by several authors (Gaviola 1950; Ringuelet 1958; Gehrz & Ney 1972; Currie et al. 1996; Smith & Gehrz 1998; Morse et al. 2001). The age of η Car’s equatorial skirt is controversial, and there is reason to suspect a mixture of material from multiple events (Smith & Gehrz 1998; Zethson et al. 1999; Morse et al. 2001; Davidson et al. 2001). The origin of the polar lobes is less ambiguous — various studies infer ejection within a few years of the Great Eruption (~ 1843). Since the polar lobes appear to be the product of a single ejection event, apparent Doppler velocities can be used to deduce their 3-D geometry. Detailed results of previous studies that used Doppler velocities of

¹ See http://www.ctio.noao.edu/instruments/ir_instruments/osiris/index.html

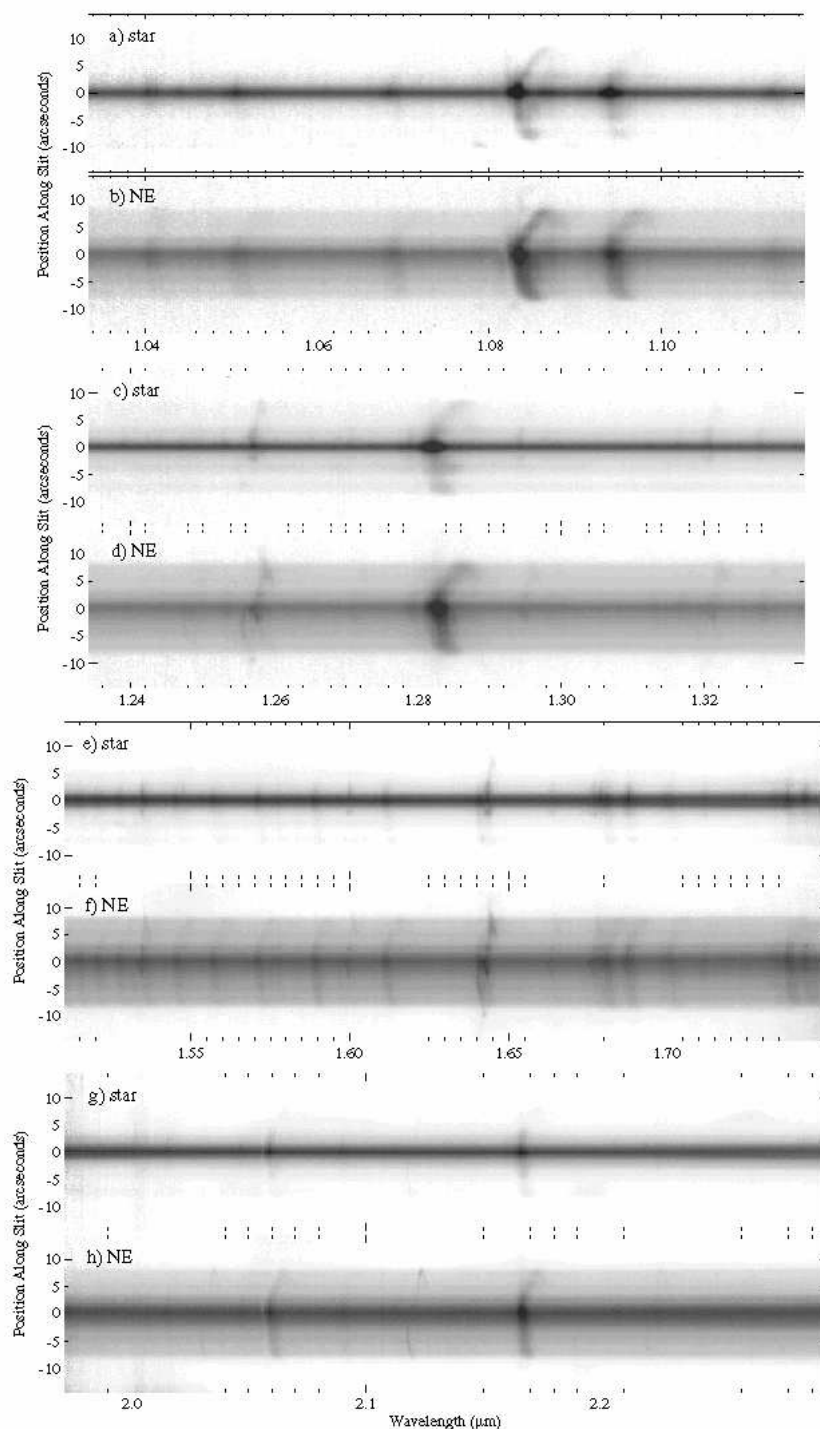


Figure 2. Grayscale representations of long-slit OSIRIS spectra with the slit centered on the star (at P.A. $=-50^\circ$), as well as one offset position to the north-east (see Figure 1). Panels (a) and (b) show spectra in the I-band for the star and the NE position, respectively. Panels (c) and (d) show spectra in the J-band, panels (e) and (f) show the H-band, and (g) and (h) show the K-band.

optical lines or polarization measurements have shown some disagreement (Thackeray 1951, 1956a, 1956b; 1961; Meaburn et al. 1987, 1993; Hillier & Allen 1992; Allen & Hillier 1993; Hillier 1997; Currie & Dowling 1999; Schulte-Ladbeck et al. 1999). A recent study using *HST*/STIS spectroscopy has improved the situation somewhat (Davidson et al. 2001). No

attempt has yet been made to investigate this using IR emission lines, where extinction is less problematic. Recently, Smith & Davidson (2001) discovered bright, IR lines from H_2 and $[Fe\ II]$ emitted by gas in the polar lobes. These lines are obvious in the spectrum near the edge of the NW lobe shown in Figure 3. Molecular hydrogen lines in particular

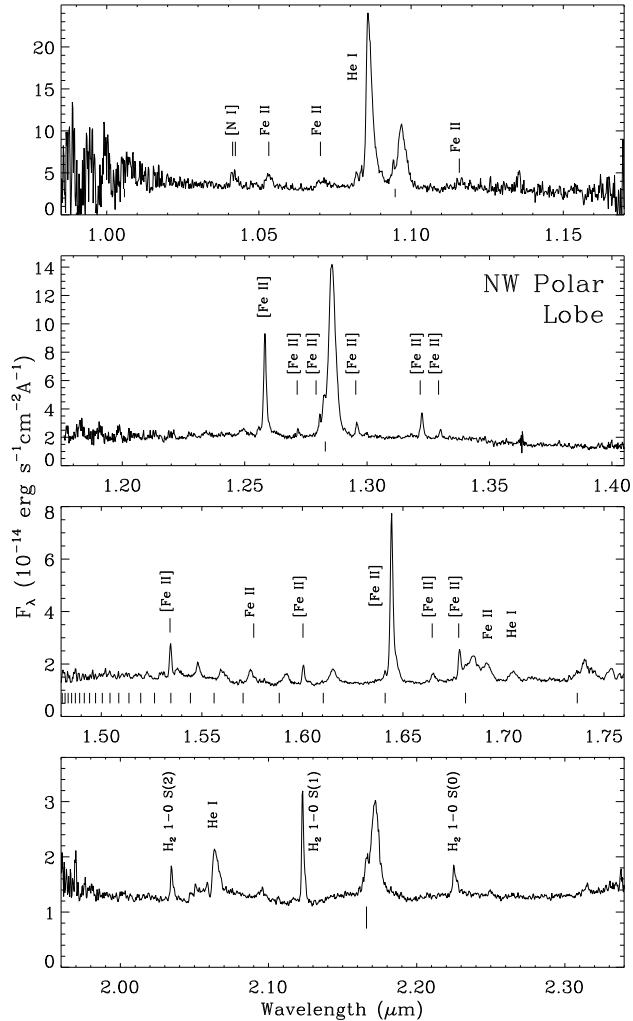


Figure 3. Near-IR spectrum near the edge of the NW polar lobe of the Homunculus, extracted from a $1''.2$ segment of the $0''.5$ -wide slit. The extraction region is centered $\sim 7''.5$ NW of the star along the NE slit position (see Figure 1). Rest wavelengths of hydrogen lines are marked with dashes below the continuum, although reflected stellar wind lines are redshifted.

are ideal for investigating the geometry, since they are *only* emitted by gas in the lobes and therefore do not suffer from confusing velocity components reflected by dust in the Homunculus, and because extinction at $2 \mu\text{m}$ is low. [Fe II] lines also provide essential information.

3.1 Emission Structure

Figure 4 shows velocity structure² as a function of position along the slit for [Fe II] $\lambda 16435$ and H_2 $v=1-0$ S(1) $\lambda 21218$. Related lines, such as [Fe II] $\lambda 12567$ and H_2 $v=1-0$ S(2) $\lambda 20338$ (see Figures 2 and 3), show similar structure but are fainter. Three slit positions are shown, with the slit crossing through the star and offset positions NE and SW.

² Continuum emission has been suppressed in Figure 4. A smooth continuum model was used for H_2 , and a segment of the H-band spectrum around Br13 was used for [Fe II] $\lambda 16435$.

Short exposure times had to be used with the slit centered on the star, so the signal-to-noise there is worse, but extended velocity structure can still be distinguished.

[Fe II] emission components in Figure 4 are complex and trace several different features in the Homunculus, but can be understood in the context of previous work (see Allen & Hillier 1993; Davidson et al. 2001; Ishibashi et al. 2003). By comparison, H_2 emission structure is surprisingly elegant, and seems to trace only material in the polar lobes. Lower extinction at IR wavelengths has allowed us to *see the back wall of the SE lobe* unambiguously for the first time in both H_2 and [Fe II]. Also, subtle differences in shape can be seen from one position to the next, especially in H_2 , and there is a conspicuous gap in the emission structure at $6''$ SE for the slit position passing through the star (Figures 4b and e). This slit also traverses an infamous “hole” in the SE lobe seen in images of the Homunculus (see Figure 1), the nature of which has been controversial (Smith et al. 1998; Morse et al. 1998; Schulte-Ladbeck et al. 1999). The fact that both [Fe II] and H_2 emission show a pronounced gap in the emission structure, combined with the fact that we apparently see the back wall of the Homunculus at the same position, has interesting implications.

The images in Figure 4 are stretched horizontally from their original pixel sampling to reflect the actual shape of the polar lobes, but the magnification factor is not arbitrary; it depends on assumed values for the heliocentric distance and ejecta age. Defining Z as the position along the line-of-sight in arcseconds, apparent Doppler velocities v in km s^{-1} yield values for Z if the age of the ejecta t_{yr} and heliocentric distance D_{pc} are known using the relation

$$Z = 0.21 \frac{v t_{\text{yr}}}{D_{\text{pc}}} \text{ arcseconds.} \quad (1)$$

Figures 5a and b show how emission structure varies with Z and position along the slit for a heliocentric distance of 2250 pc and an age of 158 years (ejection date of 1843), using the same length scale for both the vertical and horizontal axes (the same proportions were used in Figure 4 as well, although Doppler velocities were shown there). A distance of 2250 pc yielded the most symmetric appearance for the polar lobe structure in the H_2 line; assumed values of 2200 and 2300 pc were noticeably distorted. Davidson et al. (2001) found the same result for optical emission lines in *HST*/STIS data, and their quoted uncertainty of ± 50 pc is applicable here as well. Figures 5a and b show a cross section of the Homunculus in [Fe II] $\lambda 16435$ and H_2 $\lambda 21218$ emission for an average of the NE and SW slit positions.

Figures 5c and d compare the relative distribution of [Fe II] and H_2 by superimposing isophotal contours of one line’s velocity structure over grayscale images of the other. It is clear from these figures that [Fe II] emission associated with the polar lobes resides mostly interior to the H_2 . Figure 6 conveys the same conclusion with tracings of the velocity profile for each line at a few representative positions. The particular spatial distribution of these two lines, combined with the fact that neither emission line appears to exceed the confines of the polar lobes, supports an earlier contention (Smith & Davidson 2001) that this emission may arise from

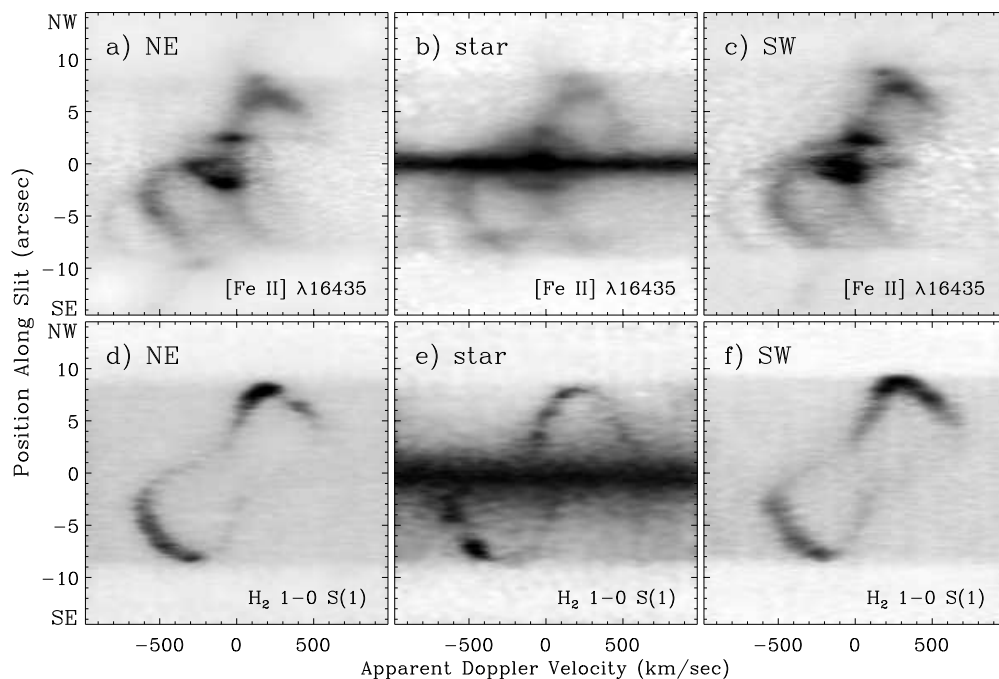


Figure 4. Details of velocity structure for three slit positions in Figure 1, for $[\text{Fe II}] \lambda 16435$ (a, b, c), and $\text{H}_2 1-0 \text{ S}(1) \lambda 21218$ (d, e, f).

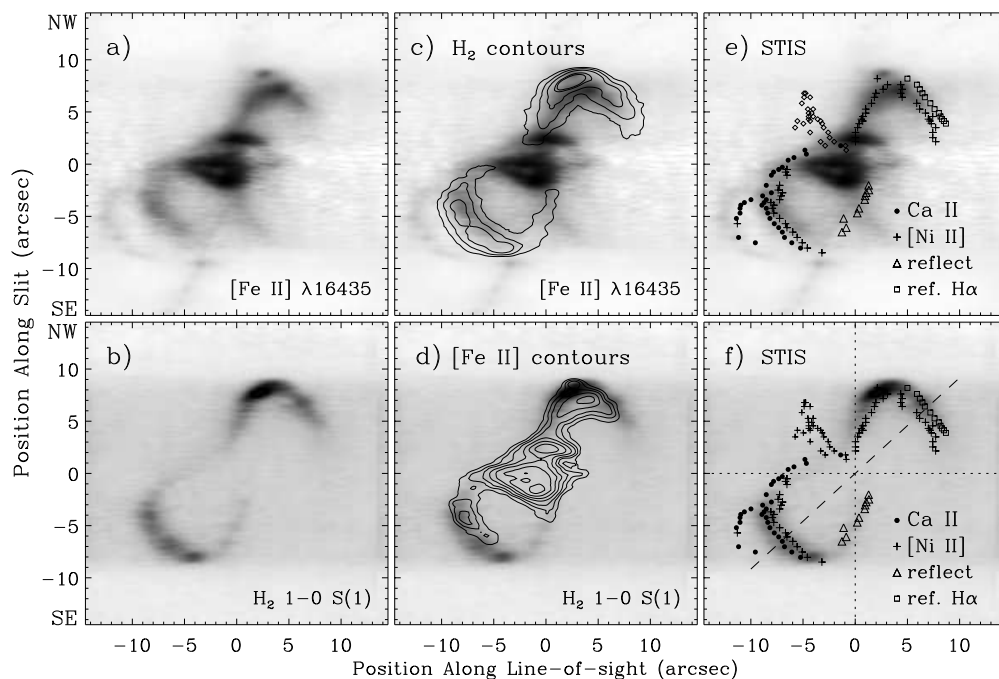


Figure 5. Panels (a) and (b) show emission-line structure for $[\text{Fe II}] \lambda 16435$ and $\text{H}_2 1-0 \text{ S}(1) 2.1218 \mu\text{m}$, respectively, with the horizontal axis scale determined using equation (1). The observed structure represents a meridional cross section of the Homunculus for an average of the NE and SW slit positions from Figure 4. Panels (c) and (d) are the same as (a) and (b), but with isophotal contours of the complementary emission line superimposed. Panels (e) and (f) are the same as (a) and (b), overlaid with points derived from velocities measured in *HST/STIS* data by the author (see also Davidson et al. 2001). The derived structure is plotted for Ca II $\lambda\lambda 3935, 3970$ absorption, $[\text{Ni II}] \lambda 7379$ emission, and reflected emission from $[\text{Ni II}]$ and $\text{H}\alpha$ corrected for expansion of reflecting dust.

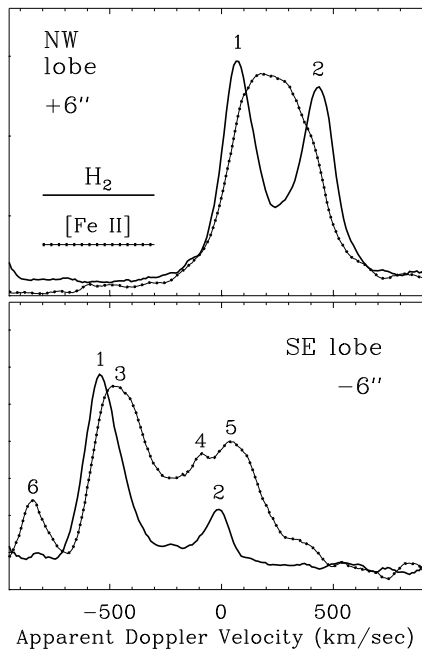


Figure 6. Tracings of H_2 $\lambda 21218$ and $[\text{Fe II}]$ $\lambda 16435$ profiles for a $0''.5$ segment along the slit at positions in the NW polar lobe (top) and the SE polar lobe (bottom). Components 1 and 2 represent H_2 emission from the front and back of the lobes, respectively. $[\text{Fe II}]$ from the front and back of the NW lobe is unresolved, but it is in the SE lobe (components 3 and 4). Component 5 is reflected emission, and component 6 corresponds to high-speed gas outside the Homunculus (see Figure 4).

a shock caused by a fast stellar wind impacting the *inside* surfaces of the polar lobes.³

Doppler velocities for optical lines in *HST*/STIS data (measured independently by the author, but see Davidson et al. 2001) have been converted to the same coordinates along the line-of-sight and plotted over the IR emission structure in Figure 5e and f. Ca II absorption in STIS data appears to overlap with infrared H_2 emission in the SE lobe in Figure 5f (some Ca II absorption also arises at high velocities in front of the SE lobe, associated with the $[\text{Fe II}]$ emission features in ejecta outside the Homunculus). $[\text{Ni II}]$ $\lambda 7379$ emission overlaps with $[\text{Fe II}]$ $\lambda 16435$ instead, and resides interior to both H_2 emission and Ca II absorption. Reflected emission lines from the back walls of the polar lobes trace dust, which seems to reside in the exterior parts of the lobes coincident with H_2 . Therefore, H_2 emission appears to be the best unambiguous tracer of the shape and orientation of the dense neutral gas and dust, while atomic emission lines arise from material inside the lobes. This is why Davidson et al.’s “model 1” derived from $[\text{Ni II}]$ $\lambda 7379$ produced a shape that was too small compared to continuum images.

³ $[\text{Fe II}]$ emission gives evidence for a shock at the *outside* surface of the polar lobe as well; there is a small emission blob at the edge of the NW lobe, seen most clearly in Figure 5a. This blob is clearly separated from $[\text{Fe II}]$ inside the NW lobe, and the gap between them corresponds precisely to the location of the H_2 emission (Figure 5c). The spectrum of this outer shock and its interesting implications will be discussed in a later publication.

Table 1. $R(\theta)$ and $V(\theta)$ for the Polar Lobes

Latitude (deg)	Radius (AU)	Velocity (km s^{-1})
5	4890	148
10	5220	158
15	5540	168
20	5980	181
25	6520	197
30	7120	215
35	8150	246
40	9670	292
45	11950	361
50	16030	485
55	17930	542
60	18800	568
65	19670	595
70	20650	625
75	21350	646
80	21140	639
85	21030	636
90	21080	637

3.2 Geometry of the Homunculus

Various models for the exact 3-D geometry of the Homunculus have been controversial, since the detailed shape of the polar lobes may hold important clues to ejection physics during the Great Eruption. The shape of the lobes depends on the tilt angle of the polar axis with respect to our line-of-sight; to avoid confusion, the inclination angle i is used as defined for binary systems, where a view from the equator is $i=90^\circ$. The inclination was measured by rotating Figure 5b so that the polar axis was nearly vertical, and then flipping the image about the horizontal and vertical axes and examining the lobe thickness when the images were added. The smallest dispersion (i.e. the most symmetric shape) was found for $i=42^\circ 5 \pm 2^\circ$. This value is only slightly larger than $i \approx 41^\circ$ found by Davidson et al. (2001), mainly because of differences in the shape of H_2 emission compared with optical lines. Smith et al. (1999) also derived $i \approx 40^\circ$ from equatorial features seen in IR images. Figure 7 shows the end result of rotating Figure 5b by $90-i$, reflecting it across the various symmetry axes, and averaging. This gives an artificially symmetric picture of the polar lobes, but it is a good approximation for discussion here. The size of the nebula is derived assuming a distance of 2250 pc and an age of 158 years. Table 1 lists representative values for the radius and expansion velocity at each latitude ($\theta=90^\circ$ at the pole).

The Homunculus shape is often discussed in the context of three geometric models, which approximate the lobes as a pair of flasks, bubbles (spheres), or bipolar caps (see Hillier 1997). None of these three models adequately describes the geometry in Figure 7, but one can see how each has a kernel of truth. One important way that Figure 7 differs from all these models is that near the equator, the walls of the polar lobes clearly do not converge on the central star. Instead, the two lobes appear meet a few thousand AU from the star. One might expect an equatorial torus to reside at the intersection of these lobes, and in fact, a structure resembling a disrupted torus is seen there in thermal-IR images (Smith et al. 2002).

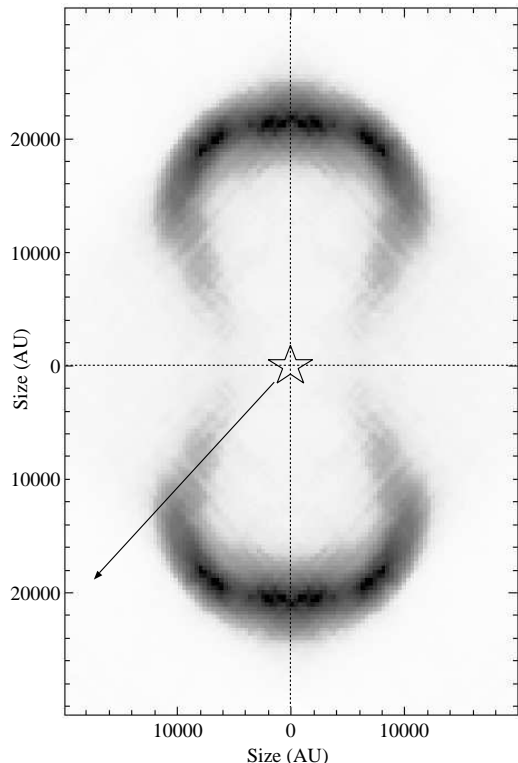


Figure 7. Meridional cross-section of the shape of the polar lobes in the Homunculus, derived by rotating the H_2 emission structure in Figure 5b counter-clockwise by $90-i$, and reflecting it about the symmetry axes. Measured parameters as functions of latitude are given in Table 1. The arrow shows the direction toward the observer. The lobes are $\sim 5\%$ smaller for a figure prepared the same way using the $[\text{Fe II}] \lambda 16435$ line (not shown).

Figure 7 seems generally consistent with hydrodynamic simulations of bipolar nebula formation applied to η Car (e.g. Frank et al. 1995, 1998; Dwarkadas & Balick 1998), and some details are as well. For instance, the scenario discussed by Frank et al. (1995) predicts two shocks – one at the inside of the polar lobes as the post-eruption wind collides with ejecta, and one on the outside as ejecta sweep up the ambient medium. $[\text{Fe II}] \lambda 16435$ shows emission from both inner and outer shocks in Figure 5, as mentioned earlier.

The observed structure does not necessarily rule out other ideas for the formation of the Homunculus. After examining the geometry of the present-day aspherical stellar wind, Smith et al. (2003) suggest that the shape of the Homunculus might have arisen from intrinsically asymmetric ejection during the Great Eruption, and may have been shaped somewhat by an asymmetric post-eruption wind. In that case, we might expect the latitudinal dependence of ejection velocity during the eruption to be related to the star’s rotation. For instance, ejection speed v_∞ at various latitudes θ may vary with escape speed on a rotating star as

$$v_\infty = v_{\text{pole}} (1 - \Omega^2 \cos^2 \theta)^{\frac{1}{2}} \quad (2)$$

where $\Omega \equiv (v_{\text{rot}}/v_{\text{esc}})$ at the equator. Expansion speeds at each latitude in Table 1 are plotted in Figure 8, with curves of equation (2) for values of Ω near critical rotation. Equation (2) provides an adequate description of the shape of

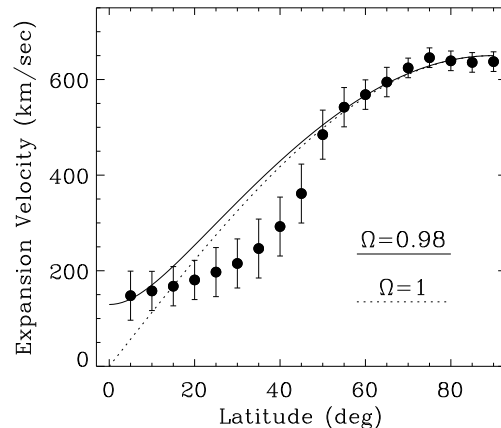


Figure 8. Expansion velocity of H_2 in the polar lobes as a function of latitude (see Table 1). Solid and dotted curves show equation (2) for two values of Ω and a polar velocity of 650 km s^{-1} .

the polar lobes at latitudes above $\theta=50^\circ$, where most of the mass was presumably ejected in thick polar caps (e.g., Hillier & Allen 1992). The walls of the polar lobes at $\theta < 50^\circ$ are optically thinner and presumably less massive; they may have been decelerated as they plowed through the ambient medium, or during a hypothetical collision with a pre-existing torus (e.g., Dwarkadas & Balick 1998).

Figures 4 and 5 also show narrow $[\text{Fe II}]$ emission from a fast outer bubble projected in front of the SE polar lobe. This outer bubble is seen at -500 to -900 km s^{-1} in $[\text{Fe II}]$, and appears at slightly lower velocities in Ca II absorption in STIS spectra (Figures 5e and f). Apparently, it also causes absorption in the $\text{He I } \lambda 10830$ line (see §6.3 and Figure 20 below). This outer feature corresponds to velocity component number 6 in tracings of $[\text{Fe II}]$ in Figure 6. Its actual 3-D structure is uncertain because its age is not known.

3.3 Excitation of the Polar Lobes

Observed fluxes from Figure 3 for several *intrinsic* emission lines in the NW polar lobe are listed in Table 2.⁴ $\text{H}_2 v=2-1$ and Q-branch transitions are absent or very weak in Figure 3; these are typically weak in molecular gas excited by shocks (e.g., Shull & Hollenbach 1978), and relatively strong $\text{H}_2 1-0 \text{ S}(1)$ emission (low excitation temperature) is conventionally taken to indicate shock excitation. Here, the $\text{H}_2 1-0 \text{ S}(1) / \text{H}_2 2-1 \text{ S}(1)$ ratio of ~ 12 implies a characteristic

⁴ Since the spectrum of the NW polar lobe is a complex mix of intrinsic emission and reflected emission lines from the stellar wind and Weigelt blobs (redshifted by almost $+1000 \text{ km s}^{-1}$), some lines in the spectrum are excluded and corrections were applied after considering kinematic information. For instance, $[\text{Fe II}] \lambda 16435$ is blended with $\text{Br}12$, and the flux for this line was adjusted accordingly in Table 2. Also, $\text{Br}\gamma$ has an intrinsic narrow component in addition to the strong reflected line from the stellar wind, but this narrow component is blueshifted and appears to be emitted by slow-moving equatorial gas (see §5). Therefore, Table 2 lists a likely upper limit to the $\text{Br}\gamma$ flux in the polar lobe.

Table 2. Intrinsic Emission-lines in the Homunculus^a

Wavelength (Å)	I.D. ^b	NW Lobe Flux (erg s ⁻¹ cm ⁻²)	LH Flux (erg s ⁻¹ cm ⁻²)	Fan Flux (erg s ⁻¹ cm ⁻²)
12567	[Fe II] (<i>a</i> ⁶ <i>D</i> - <i>a</i> ⁴ <i>D</i>)	7.22×10 ⁻¹³	5.80×10 ⁻¹²	1.94×10 ⁻¹¹
12788	[Fe II] (<i>a</i> ⁶ <i>D</i> - <i>a</i> ⁴ <i>D</i>)	4.83×10 ⁻¹⁴	7.92×10 ⁻¹³	3.28×10 ⁻¹²
12818	H I Paβ	(<4×10 ⁻¹⁵)	(<2×10 ⁻¹⁴)	2.69×10 ⁻¹¹
12943	[Fe II] (<i>a</i> ⁶ <i>D</i> - <i>a</i> ⁴ <i>D</i>)	8.84×10 ⁻¹⁴	9.65×10 ⁻¹³	3.06×10 ⁻¹²
13205	[Fe II] (<i>a</i> ⁶ <i>D</i> - <i>a</i> ⁴ <i>D</i>)	2.23×10 ⁻¹³	1.13×10 ⁻¹²	3.91×10 ⁻¹²
15335	[Fe II] (<i>a</i> ⁴ <i>F</i> - <i>a</i> ⁴ <i>D</i>)	1.57×10 ⁻¹³	1.27×10 ⁻¹²	6.96×10 ⁻¹²
15995	[Fe II] (<i>a</i> ⁴ <i>F</i> - <i>a</i> ⁴ <i>D</i>)	9.92×10 ⁻¹⁴	1.33×10 ⁻¹²	5.71×10 ⁻¹²
16435	[Fe II] (<i>a</i> ⁴ <i>F</i> - <i>a</i> ⁴ <i>D</i>)	1.05×10 ⁻¹²	7.92×10 ⁻¹²	1.89×10 ⁻¹¹
16637	[Fe II] (<i>a</i> ⁴ <i>F</i> - <i>a</i> ⁴ <i>D</i>)	7.44×10 ⁻¹⁴	5.43×10 ⁻¹³	2.64×10 ⁻¹²
16769	[Fe II] (<i>a</i> ⁴ <i>F</i> - <i>a</i> ⁴ <i>D</i>)	1.39×10 ⁻¹³	1.18×10 ⁻¹²	7.83×10 ⁻¹²
16787	Fe II (<i>z</i> ⁴ <i>F</i> - <i>c</i> ⁴ <i>F</i>)	...	1.25×10 ⁻¹³	6.92×10 ⁻¹²
16873	Fe II (<i>z</i> ⁴ <i>F</i> - <i>c</i> ⁴ <i>F</i>)	...	2.68×10 ⁻¹³	9.25×10 ⁻¹²
17111	[Fe II] (<i>a</i> ⁴ <i>F</i> - <i>a</i> ⁴ <i>D</i>)	...	7.92×10 ⁻¹³	1.26×10 ⁻¹²
17414	Fe II (<i>z</i> ⁴ <i>F</i> - <i>c</i> ⁴ <i>F</i>)	...	4.56×10 ⁻¹³	7.67×10 ⁻¹²
19572	Fe II (<i>z</i> ⁴ <i>F</i> - <i>c</i> ⁴ <i>F</i>)	6.61×10 ⁻¹²
19746	Fe II (<i>z</i> ⁴ <i>F</i> - <i>c</i> ⁴ <i>F</i>)	...	2.90×10 ⁻¹³	2.31×10 ⁻¹²
20151	[Fe II] (<i>a</i> ² <i>G</i> - <i>a</i> ² <i>H</i>)	...	5.33×10 ⁻¹³	1.94×10 ⁻¹²
20338	H ₂ 1-0 S(2)	1.36×10 ⁻¹³
20460	[Fe II] (<i>a</i> ⁴ <i>P</i> - <i>a</i> ² <i>P</i>)	...	6.08×10 ⁻¹³	1.50×10 ⁻¹²
20581,600	He I, Fe II (<i>z</i> ⁴ <i>F</i> - <i>c</i> ⁴ <i>F</i>)	...	3.74×10 ⁻¹³	3.61×10 ⁻¹²
20888	Fe II (<i>z</i> ⁴ <i>F</i> - <i>c</i> ⁴ <i>F</i>)	2.20×10 ⁻¹⁴	3.49×10 ⁻¹³	2.96×10 ⁻¹²
21218	H ₂ 1-0 S(1)	4.17×10 ⁻¹³
21655	H I Brγ	(<4×10 ⁻¹⁵)	(<3×10 ⁻¹⁴)	5.49×10 ⁻¹²
22233	H ₂ 1-0 S(0)	1.51×10 ⁻¹³
22477	H ₂ 2-1 S(1)	1.77×10 ⁻¹⁴

^aSee Figures 3, 10, and 11. If more than one wavelength is given, the line is blended, and both lines are expected to contribute significantly.

^bJ subscripts for Fe⁺ lines have been omitted.

excitation temperature of ~ 2000 K. This rules out *radiative* fluorescence (i.e. direct excitation through absorption in the Lyman and Werner bands in the UV) as the excitation mechanism for the H₂, since that mechanism results in a H₂ 1-0 S(1) / H₂ 2-1 S(1) ratio of ~ 2 (Sternberg & Dalgarno 1989). However, Sternberg & Dalgarno (1989) point out that *collisional* fluorescent emission can also result in low excitation temperatures ($\sim 10^3$ K) in dense molecular gas irradiated by a strong UV flux. Sternberg & Dalgarno stress that collisional excitation of dense gas resulting from radiative heating can mimic line ratios in shocks.

A similar conundrum may exist for the excitation mechanism of [Fe II] lines at 12567 and 16435 Å. Models for IR emission from dense interstellar shocks (e.g., McKee, Chernoff, & Hollenbach 1984) predict enhanced [Fe II] compared to H. Observationally, shock-excited gas such as that in supernova remnants shows high ratios of [Fe II] $\lambda 16435$ /Br $\gamma \gtrsim 30$ (Graham et al. 1987; Oliva et al. 1990; Seward et al. 1983), whereas H II regions have [Fe II] $\lambda 16435$ /Br $\gamma \lesssim 1$ (Moorwood & Oliva 1988; Mouri et al. 1990). The observed [Fe II] $\lambda 16435$ /Br γ ratio in the NW polar lobe is >26 (Table 3), which would conventionally be interpreted as a shock. However, radiation may be able to heat the gas to a few 10^3 K as well, allowing collisionally-excited [Fe II] lines and still suppressing the H recombination lines. For instance, the Crab Nebula has a high [Fe II] $\lambda 16435$ /Br γ ratio ranging from 10 to 50 (Graham et al. 1990), and it is photoexcited by a power-law synchrotron spectrum. The excitation of this warm gas in the polar lobes of η Car will be investigated quantitatively by Ferland, Davidson, & Smith (2002).

In any case, it seems clear from Figure 5 that [Fe II] emission arises at the *inside* surface of the hollow polar lobes; peaks in H₂ and [Fe II] are separated by ~ 1000 AU. The separation of H₂ and [Fe II] emission may have implications for grain destruction and the gas-phase iron abundance in this photodissociation region.

[Fe II] $\lambda 12567$ and $\lambda 16435$ share the same upper level, and atomic physics predicts an intrinsic flux ratio of $\lambda 12567/\lambda 16435 \approx 1.36$ (Nussbaumer & Storey 1988). The observed flux ratio less than 1 in Table 3 therefore indicates considerable reddening from circumstellar dust in the walls of the polar lobes; however, the reddening law for dust in the Homunculus is anomalous and poorly constrained, so it is not possible to extrapolate this ratio to A_V .

If η Car lost $\sim 2 M_\odot$ during the Great Eruption (Smith et al. 1998), then the particle density in the polar lobes today should be on the order of $10^{4.5}$ to 10^5 cm⁻³, given the apparent thickness and radii of the lobes in IR images (Smith et al. 1998; 2002). Therefore, the density is within the regime for collisional fluorescence of H₂ discussed by Sternberg & Dalgarno (1989). The [Fe II]-emitting region seems to be spatially segregated from H₂, and the electron density there can be estimated from ratios of some infrared [Fe II] lines with weak temperature dependence that are all collisionally excited *a*⁴*F*-*a*⁴*D* transitions with closely spaced energy levels near the ground state. Following Nussbaumer & Storey (1980; 1988), Table 3 lists values for n_e derived from the diagnostic line ratios [Fe II] $\lambda 15335/\lambda 16435$, $\lambda 15995/\lambda 16435$, and $\lambda 16637/\lambda 16435$. The average of these is $\sim 10^{4.1}$ cm⁻³ in the polar lobes, close to the expected value mentioned

Table 3. Nebular Densities and Line Ratios

Diagnostic	NW Lobe	LH	Fan	Weigelt blobs
$\log n_e$ ($\frac{15335}{16435}$) ^a	4.0	4.0	> 5.3	> 5.8
$\log n_e$ ($\frac{15935}{16435}$) ^a	3.9	4.4	> 5.4	> 5.6
$\log n_e$ ($\frac{16435}{16637}$) ^a	4.2	4.2	> 5.0	> 5.8
$\log n_e$ (average)	4.1	4.2	> 5.3	> 5.6
$\lambda 16435/\text{Br}\gamma$	> 26	> 26	3.4	0.74
$\lambda 12567/\lambda 16435$	0.7	0.7	1.0	0.99

^aSee Nussbaumer & Storey (1980, 1988).

above. This implies that [Fe II] in the lobes arises in ejecta from the Great Eruption, rather than post-eruption wind.

4 THE LITTLE HOMUNCULUS

Ishibashi et al. (2003) discovered a bipolar nebula expanding inside the Homunculus, based on spatially-resolved *HST*/STIS spectroscopy. Proper motions of structures in those data indicate that this ‘Little Homunculus’ seems to have an age of ~ 100 years, perhaps ejected during the minor eruption of η Carinae in 1890. The Little Homunculus (LH) can also be seen in some IR emission lines like [Fe II] $\lambda 12567$ and $\lambda 16435$ (Figure 9). The bipolar shape of the LH in [Fe II] $\lambda 16435$ is more prominent than in optical spectra because collisionally-excited IR lines like [Fe II] $\lambda 16435$ are so bright, and because extinction from the SE lobe is less severe in the IR. The hollow structure of the LH’s blueshifted SE lobe is clear, but the NW polar lobe of the LH is fainter. Equatorial dust seen in thermal-IR images (Smith et al. 2002) may block light from the far side of the LH. Polar ejecta in the LH expand at speeds around 200 km s^{-1} in Figure 9. Walborn & Liller (1977) pointed out that during the 1890 eruption, absorption features were seen at -200 km s^{-1} in η Car’s spectrum (Whitney 1952). This supports Ishibashi et al.’s claim that the LH may have originated in that event.

Figure 10 shows the IR spectrum at the brightest position in the LH, indicated by the arrow in Figure 9. [Fe II] lines are enhanced, and most show a blueshifted component at about -500 km s^{-1} from the SE lobe of the Homunculus. H lines in Figure 10 are reflected from the wind and Weigelt blobs, and are not relevant to the LH itself. Table 2 lists intensities for emission arising in the LH; emission components from the Homunculus (including H_2) and reflected wind lines are excluded.

The LH spectrum is qualitatively similar to the spectrum of the NW polar lobe, except that H_2 emission is absent here. Most infrared [Fe II] lines in the LH spectrum arise from one of two multiplets ($a^4F - a^4D$ or $a^6D - a^4D$), which are collisionally-excited transitions with an upper level 1 eV from the ground state. The [Fe II] $\lambda 16435/\text{Br}\gamma$ ratio is quite high, like that seen in the NW polar lobe (see Table 3), and comments about the excitation mechanism described there may apply. However, an important difference is that the LH seems to lack bright thermal-IR emission from dust (Smith et al. 2002), as well as H_2 . A contribution from photoexcitation in the LH cannot be ruled out, but the spectrum of the LH definitely lacks strong intrinsic IR emission arising from Fe II transitions pumped by UV fluorescence (see §5.1), which are prominent in some other ejecta near η Car.

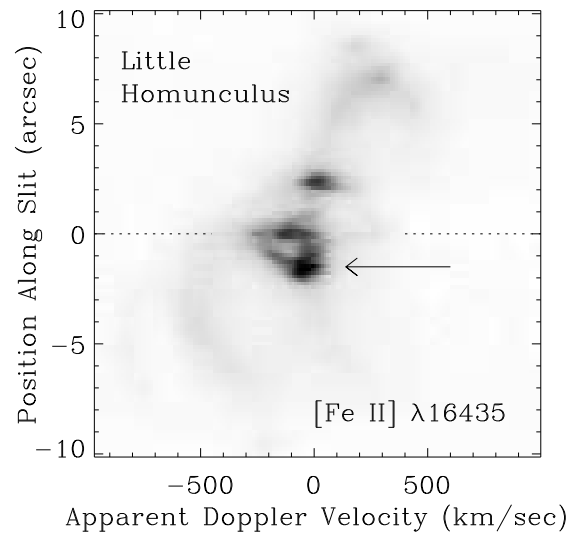


Figure 9. Same as Figure 5a, with the display chosen to highlight bright [Fe II] $\lambda 16435$ emission from the ‘Little Homunculus’. Apparent Doppler velocities are shown, but the horizontal scale is stretched by a factor corresponding to an ejection date of 1890 (see equation 1). The arrow shows the location of the extracted spectrum shown in Figure 10.

The [Fe II] $\lambda 12567/\lambda 16435$ ratio in the LH is nearly the same as for the NW lobe (Table 3), and so both suffer similar reddening from dust in the lobes. As with the polar lobe spectrum, ratios of certain [Fe II] lines from the $a^4F - a^4D$ multiplet are useful for estimating the electron density in the LH, which appears to be $\sim 10^{4.2} \text{ cm}^{-3}$ (Table 3).

5 PECULIAR EQUATORIAL EMISSION

It is interesting that both the LH and the polar lobes of the larger Homunculus show strong intrinsic emission in collisionally-excited lines. These same tracers of collisional excitation are not seen in emission from equatorial gas, which would be projected in front of the NW lobe in Figures 4, 5, and 9. However, some lines do show interesting evidence for blueshifted equatorial emission, providing insight to the nature of η Car’s equatorial ejecta.

5.1 IR Spectrum of the Fan

Optical continuum images (Morse et al. 1998) show a prominent feature extending a few arcseconds NW of the star, called the ‘Fan’, and it *looks* as if it is part of an equatorial spray. However, thermal-IR images reveal that the Fan is actually the dust column-density minimum in the equatorial ejecta and it appears to be a hole where we see through to the NW lobe (Smith et al. 1999, 2002). This hole may also allow UV photons to escape to larger radii and excite equatorial gas. Part of the Fan shows blueshifted emission with unusual excitation and strange kinematics (e.g., Zethson et al. 1999; Johansson et al. 2000), as well as some emission lines like [Sr II] that are not seen anywhere else in the Homunculus (Hartman et al. 2001; Zethson et al. 2001).

Figure 11 shows the near-IR spectrum at one position in

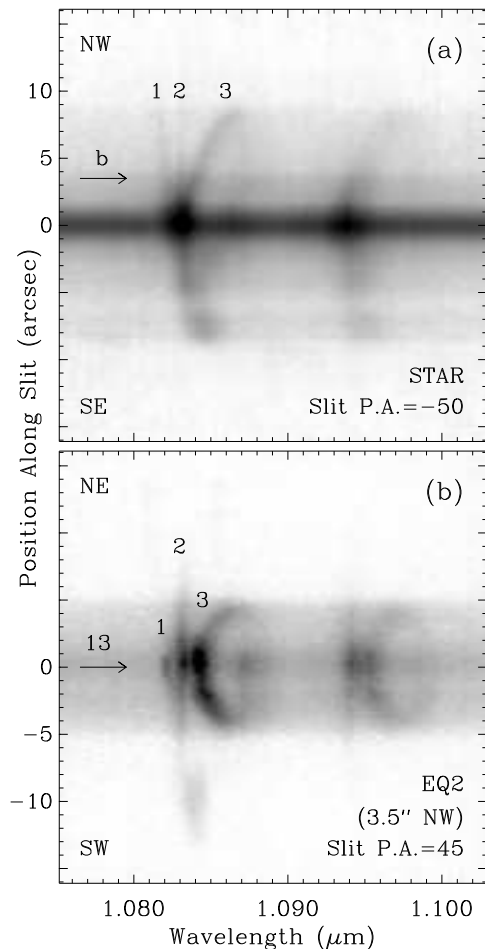


Figure 12. Long-slit OSIRIS spectra showing He I $\lambda 10830$ and Pa γ . Panel (a) is a segment of Figure 2a with the slit passing through the star at P.A. = -50° . The arrow identifies the location $3''.5$ NW of the star where this slit intersects that used to obtain the long-slit spectrum shown in panel (b), obtained at slit position ‘EQ2’. The numbers 1 to 3 in both panels refer to velocity components discussed in the text (§5) and shown in Figure 13.

the conjecture from the $\lambda 16435/\text{Br}\gamma$ ratio that photoexcitation dominates the Fan’s spectrum, rather than collisions. More importantly, it appears that *the peculiar fluorescent Fe II lines are bright in equatorial gas, but are absent or weak in polar ejecta.*

5.2 An Extended Equatorial Disk?

Near-IR spectra reveal some important clues about the kinematics of η Car’s equatorial ejecta seen projected in front of the NW polar lobe with blueshifted velocities. The bright H $_2$ and [Fe II] emission lines discussed earlier did not show equatorial emission, but Figure 12 shows equatorial gas in other lines, such as He I $\lambda 10830$. Figure 12a shows the kinematic structure of He I $\lambda 10830$ and Pa γ along the slit oriented parallel to the major axis of the Homunculus at P.A. = -50° (see Figure 1). Toward the NW of the star, the He I line clearly branches into three separate components, labeled 1, 2, and 3 in Figure 12a. These components are also clearly

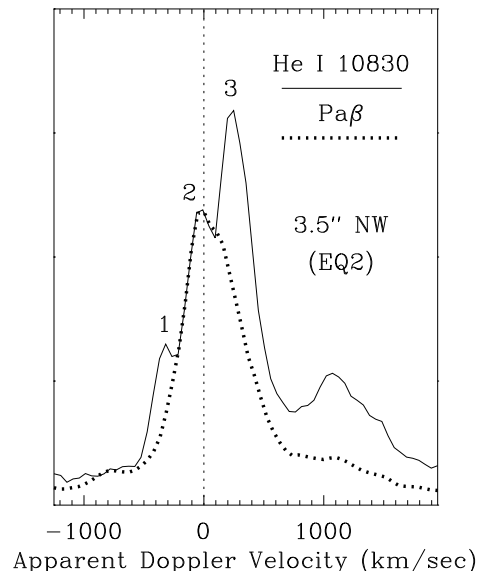


Figure 13. Profile of He I $\lambda 10830$ extracted from a $1''$ segment of Figure 12b, at the position of the arrow labeled ‘13’ in that figure, with the slit at position ‘EQ2’. Velocity components 1, 2, and 3 refer to features identified in Figure 12. The red bump at $+1100 \text{ km s}^{-1}$ is a combination of redshifted He I emission and Fe II $\lambda\lambda 10863, 10872$. The dotted line shows the profile of Pa β observed at the same position.

seen and labeled in Figure 12b, which shows a long-slit spectrum with the slit orthogonal to the polar axis (slit position ‘EQ2’ in Figure 1). From Figures 12a and b, it is clear that component 3 corresponds to light from the star reflected by expanding dust in the polar lobes, and will not be discussed further.⁵ Component 2 extends across and beyond the edges of the Homunculus in Figures 12a and b at an almost constant low velocity. It is not seen toward the SE of the star; presumably component 2 resides near the equator, and the far side is blocked by dust in the SE polar lobe.

Component 1 is only seen in He I $\lambda 10830$. It is narrow, blueshifted, and has linearly increasing speed with distance (a Hubble flow). It most likely resides in the equatorial plane. Component 1 extends to (and probably beyond) the edge of the NW polar lobe in Figure 12a, but Figure 12b reveals that it is confined to a narrow range of azimuthal angles associated with the Fan. Component 1 coincides spatially with the ‘purple haze’ seen in *HST*/WFPC2 images (Morse et al. 1998). Since the Fan is probably caused by a hole in the equatorial ejecta (Smith et al. 1999; 2002), it might allow a beam of UV starlight to escape to large radii in a disk and thereby excite the He I line. Note that component 2 shows H recombination emission, but component 1 does not. Thus, components 1 and 2 might occupy separate regions of space along different lines-of-sight to the central star.

Figure 13 shows a tracing of the He I $\lambda 10830$ line at $3''.5$ NW of the star in the Fan. Three velocity components are quite distinct at this location, with velocities of -325 , -35 , and $+290 \text{ km s}^{-1}$ for components 1, 2, and 3, respectively.

⁵ However, note that reflected He I $\lambda 10830$ emission from the far wall of the NW polar lobe affects Fe II $\lambda\lambda 10863, 10872$.

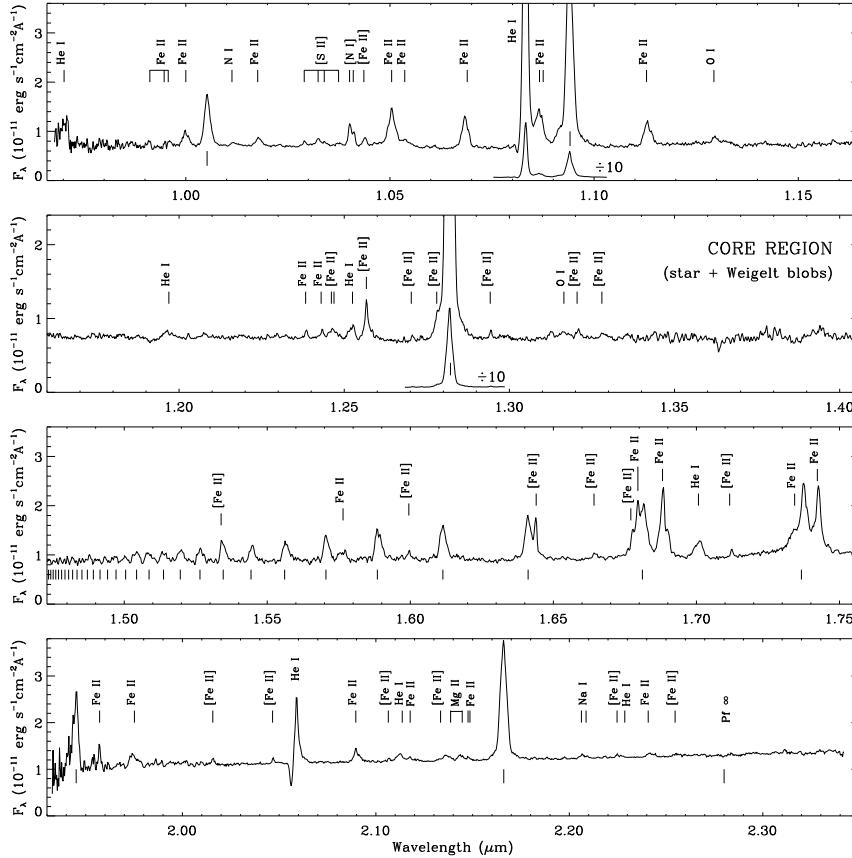


Figure 14. Spectrum of the bright core region of the Homunculus, extracted from a $0''.5$ segment of the $0''.5$ -wide slit aperture. This includes the spectrum of the central star and Weigelt blobs, but excludes emission from the Homunculus and Little Homunculus.

Uncertainty in wavelength calibration is $\pm 20 \text{ km s}^{-1}$, but relative velocities are reliable to within $\pm 5 \text{ km s}^{-1}$.

With a known inclination $i=42.5^\circ$ derived in §3, the age t in years for *equatorial* gas with a given Doppler velocity v (km s^{-1}) can be inferred as a function of projected separation from the star r in arcsec (with linear motion) using

$$t = \frac{4.74 r D \tan i}{v} \quad (3)$$

where D is the heliocentric distance in pc. Thus, at $3''.5$ NW of the star, component 1 at -325 km s^{-1} has a probable age of only 105 ± 7 years — perhaps ejected during the minor eruption of η Car in 1890. If component 2 traces slow gas near the equator, it may indicate older material with an age around 1000 years. Component 3 is not directly emitted by equatorial gas, as noted above, so equation (3) is inapplicable. Figure 13 shows that component 1 is not seen in hydrogen lines, but $\text{Pa}\beta$ from component 2 agrees quite well with He I emission. Interestingly, neither He I $\lambda 10830$ nor Paschen lines show evidence for an equatorial component originating in the Great Eruption.

These results might seem at odds with the conclusions of Zethson et al. (1999), but the new inclination angle $i=42.5^\circ$ derived in §3 affects the strange radial velocities observed by those authors. At a particular position in the Fan at $1''.3$ NE of the star (their ‘Dsk 1’), Zethson et al. measured three velocity components at -136 , -81 , and -42 km s^{-1} . An incorrect value of $i \approx 35^\circ$ assumed at that time led them to infer

ages of 160, 280, and 620 years, respectively. However, with $i=42.5^\circ$, Zethson et al.’s velocity components at -136 and -81 km s^{-1} would imply ejection during the 1890 outburst and the Great Eruption of η Car, respectively (see their Table 6). Having derived a similar inclination angle of $i=41^\circ$, Davidson et al. (2001) found two velocity components in the Fan consistent with ejection during the 1890 outburst and Great Eruption as well. Thus, the new inclination and structure of the Homunculus seem to partly resolve some problematic kinematics of the equatorial ejecta, and also support the presence of material younger than the Great Eruption. So far, this younger equatorial material from the 1890 outburst seems to be seen only in emission lines, while proper motions with *HST* images that trace primarily scattered continuum light do not detect it (Morse et al. 2001).

6 THE STAR’S SPECTRUM: DIRECT AND SCATTERED LIGHT

6.1 The Central Core

Figure 14 shows the flux-calibrated spectrum of the bright central core of the Homunculus taken through a $0''.5 \times 0''.5$ aperture in March 2001 during η Car’s high-excitation state. It is essentially the combined spectrum of direct stellar light and the nearby Weigelt blobs included in the aperture. Figure 14 resembles the IR spectrum with the same spectral

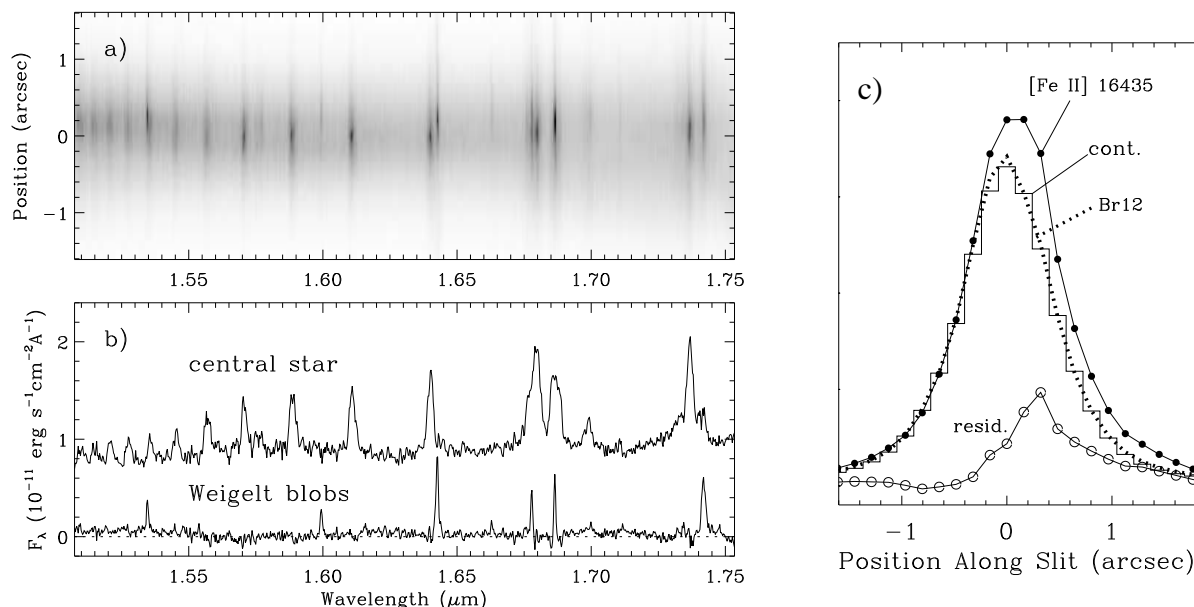


Figure 15. Panel (a) shows a portion of Figure 2e concentrating on the inner few arcseconds near the star. Some narrow lines show real positional offsets from the center. $0''.8$ -wide spectral extractions to either side of zero were made. Panel (b) shows residual emission after subtracting scaled versions of these extractions from one another, separating the spectra of the Weigelt blobs and central star. (c) Spatial scans of [Fe II] $\lambda 16435$ (filled circles), Br12 (dotted line), and adjacent continuum (histogram). Continuum emission was normalized to the Br12 emission. Unfilled circles show residuals of subtracting the continuum from [Fe II] emission.

resolution presented by Hamann et al. (1994), who used a larger $4''.8 \times 4''.8$ aperture. Detailed differences exist between Hamann et al.'s spectrum and Figure 14, but it is uncertain if they are due to temporal variability or aperture-size effects. Important changes have occurred since 1990 when Hamann et al. obtained their spectrum, and a $\sim 5''$ aperture certainly includes extended emission. The contribution of compact ejecta and reflected light are examined below.

One detail worth mentioning here (with some bearing on η Car's variability) concerns how the strength of He I $\lambda 10830$ varies with position or aperture size. Measured in a small $0''.5$ aperture, the bright central core region has a He I $\lambda 10830$ equivalent width of $\sim 205 \text{ \AA}$ in Figure 14. Farther out in the polar lobes, the He I $\lambda 10830$ equivalent width is significantly less; 125 \AA in the NW lobe and 135 \AA in the SE lobe. Independently, A. Daminieli has been monitoring η Car's He I $\lambda 10830$ line over the past several years as seen in ground-based spectra with a larger aperture (a few arcsec). His measurements⁶ give an equivalent width roughly 15-20% less than in Figure 14 at nearly the same time. Thus, the strength of this line is somewhat diluted in a large aperture that includes more extended emission.

6.2 Resolving the Spectrum of the Weigelt Blobs

High-resolution imaging has resolved the bright core of the Homunculus into a star plus three bright ejecta blobs within $0''.3$ (Weigelt & Ebersberger 1986; Hofmann & Weigelt 1888; Weigelt et al. 1995; Morse et al. 1998). These 'Weigelt blobs' have a narrow emission-line spectrum different from the

central star, and probably reside near the equator (Davidson et al. 1995; 1997). Emission from the Weigelt blobs is marginally resolved in the near-IR spectra presented here, allowing their combined spectrum to be separated from the central star for the first time at IR wavelengths. Figure 15a shows a long-slit spectrum in the H-band, concentrating on the inner few arcseconds near the star. A few narrow emission lines seem to be offset from the star's position. Figure 15c confirms this suspicion and proves that [Fe II] emission from the Weigelt blobs is marginally resolved. Residual emission after subtracting the continuum emission from [Fe II] has a centroid offset $0''.2$ to $0''.4$ from the star, as expected.

Thus, it is possible to separate these blobs from the star by extracting segments along the slit on either side of the star's position. To the NW the emission is dominated by the blobs, and to the SE the star dominates. Figure 15b shows spectra of the Weigelt blobs and star, after subtracting the adjacent component.⁷ The uncontaminated spectrum of the central star in Figure 15b shows only broad permitted lines from the stellar wind, as expected following previous results with *HST* (Davidson et al. 1995, 1997). In general, Figure 15b separates broad wind lines from narrow nebular lines. In some cases this applies to two components of the same emission line; Fe II $\lambda 16873$ is a salient example.

Figure 16 shows the full near-IR spectrum of the Weigelt blobs, produced the same way as Figure 15b. It differs from previously published IR spectra of η Car (Hamann et al. 1994), with only narrow emission lines. Table 4 lists fluxes

⁷ The true spectrum of the Weigelt blobs will include starlight scattered by dust in the blobs themselves, but that has been subtracted here in addition to instrumental scattering.

⁶ <http://www.igusp.usp.br/~daminieli/etacar/index.html>

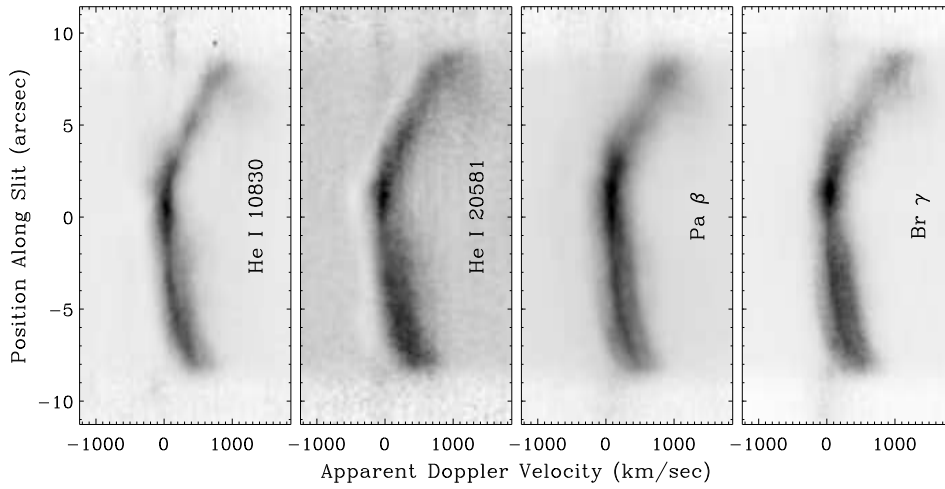


Figure 17. Long-slit spectra for reflected stellar-wind emission lines as a function of position in the Homunculus, corresponding to the NE slit position (see Figure 1). As previously, negative offsets are toward the SE, and positive offsets are NW along the slit.

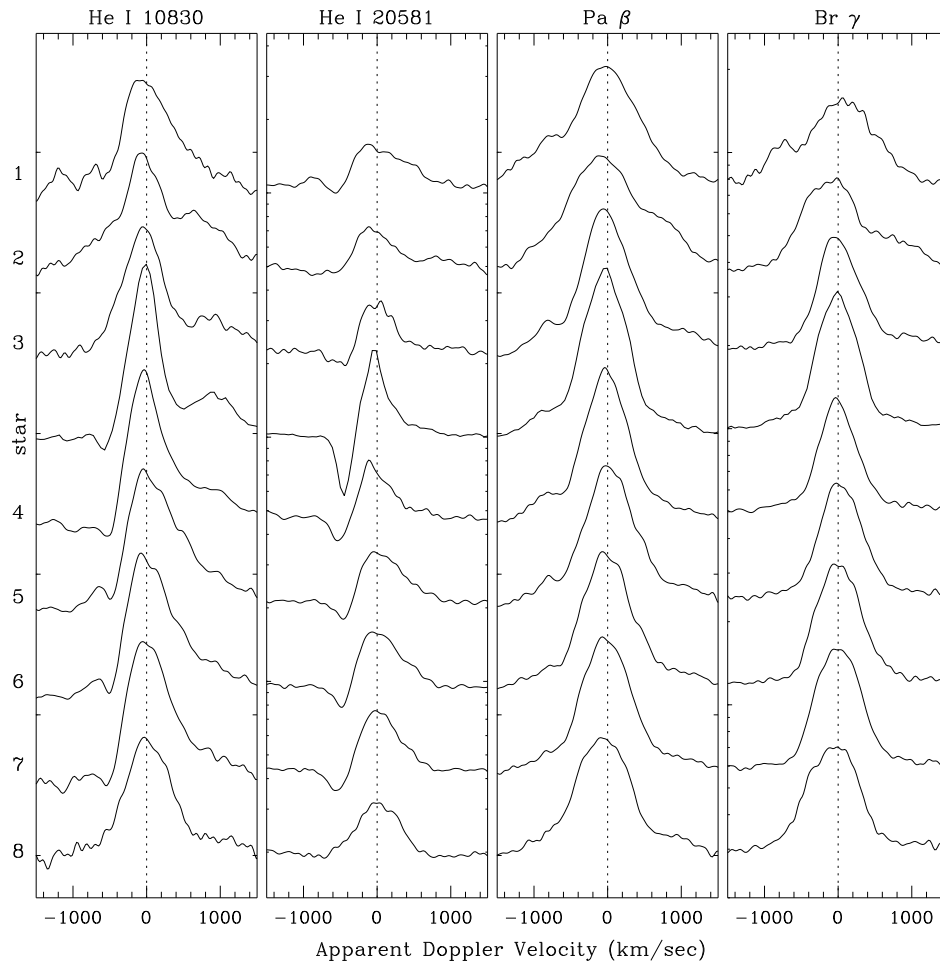


Figure 18. Tracings of line profiles for He I λ 10830, λ 20581, Pa β , and Br γ from Figure 17 at various positions along the slit (labeled at left; see Table 5). Line profiles of the bright central core (star + Weigelt blobs) from Figure 14 are also included.

Table 5. Reflected Line-Profile Extractions^a

Position	Position (arcsec)	ΔV (km s ⁻¹)	Latitude ^b (deg)
1	NW 7.5	830	58
2	NW 5.5	480	47
3	NW 2.6	165	26
STAR	0	0	48
4	NE 1.0	75	45
5	SE 2.4	120	63
6	SE 4.0	190	72
7	SE 5.7	240	83
8	SE 8.0	430	71

^aSee Figure 18.^bUncertainty in latitude is at least $\pm 5^\circ$.

in circumstellar gas. However, so far reflected spectra have only been published for wavelengths below $1 \mu\text{m}$.

Figure 17 shows details of the velocity structure at the NE slit position for four reflected stellar-wind emission lines: He I $\lambda 10830$, He I $\lambda 20581$, Pa β , and Br γ , and Figure 18 shows tracings of the velocity profiles for these lines at several different offset positions listed in Table 5. Representative latitudes for these reflected spectra are also listed in Table 5, derived from the structure of the polar lobes in §3. Figure 19 shows line profiles for the central star and reflected light at a few representative positions in the Homunculus, but normalized to the same continuum level and superimposed on one another. The position $1''$ NE of the star is chosen to show reflected light from the star at nearly the same latitude as our direct line-of-sight, and the positions in the SE and NW polar lobes are chosen to represent reflected light as seen from high and low latitudes in the stellar wind, respectively.

Hydrogen lines (Pa β and Br γ). Near-IR hydrogen lines show nearly symmetric, pure emission profiles at all latitudes, with minor variations in line shapes. Balmer lines, on the other hand, exhibit strong latitudinal dependence of P Cygni absorption (Smith et al. 2003). With the spectral resolution used here, near-IR hydrogen lines cannot offer definite constraints on the wind geometry, but they support the hypothesis that asymmetry seen in Balmer absorption (formed farther out in the wind) is due to an ionization/recombination imbalance caused by a density enhancement in the polar wind (see Smith et al. 2003).

Helium lines. Unlike He I recombination lines at optical wavelengths, He I lines at 10830 and 20581 Å show P Cygni absorption at all viewing angles except some positions in the NW lobe contaminated by equatorial emission (see §5.2). Tracings of reflected He I $\lambda 20581$ in Figures 18 and 19 show that the star has much deeper absorption than any reflected positions, even positions at roughly the same latitude; perhaps this is a radiative transfer effect similar to the excess emission seen in direct light from the central star at both optical and IR wavelengths (see Smith et al. 2003 and below). Tracings of reflected He I $\lambda 20581$ show weak latitudinal dependence in P Cyg absorption at about -550 km s^{-1} , but the He I $\lambda 10830$ absorption structure seen in the long-slit spectrum in Figure 20 is quite remarkable. The complex blueshifted He I $\lambda 10830$ absorption in Figure 20 may be a combination of P Cygni absorption in the stellar wind at velocities of roughly -550 km s^{-1} , plus nebular absorption

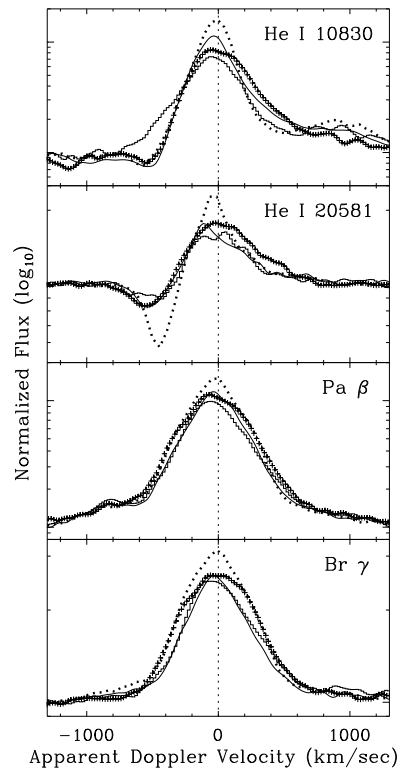


Figure 19. Selected tracings from Figure 18 for direct light from the central star (dotted line), overplotted with profiles seen in reflected light from the SE lobe at position 7 (crosses), the NW lobe at position 3 (histogram), and $1''$ NE of the star at position 4 (thin solid line). See Table 5 for more details.

from a shell outside the Homunculus, analogous to the Ca II absorption mentioned earlier. The fast blueshifted absorption has a kinematic structure and radial velocity similar to the outer bubble seen in [Fe II] $\lambda 16435$ in Figures 4 and 5. Thus, this outer nebular material may be responsible for the high-speed blueshifted absorption in the $\lambda 10830$ line seen by Damiani et al. (1998), rather than a fast component of the stellar wind. It may also cause the fast blueshifted absorption component seen in some UV resonance lines by Viotti et al. (1989). There is fast ($\sim 1000 \text{ km s}^{-1}$) material in η Car's wind, but so far it has only been detected in reflected Balmer lines (Smith et al. 2003).

Reflected emission peaks for both H and He I lines have comparable strengths at various latitudes, and all are weaker than the peak emission for lines seen in direct light from the central star. This effect is significant – line profiles in Figure 19 are plotted with a *logarithmic* vertical axis. The same effect has been noted for optical lines in η Car, and does not yet have a suitable explanation (Smith et al. 2003).

Another trait shown by both He I and H line profiles in Figure 19 is that reflected lines seen in the SE polar lobe (crosses) are always broader and extend farther toward the red than reflected lines seen in the NW polar lobe (histogram). This is also apparent in Figures 17 and 20, and is consistent with the behavior of optical He I lines and the geometry they imply (Smith et al. 2003); Balmer emission lines do not show this trend. Thus, infrared He I and H lines may trace a deep and important region of the wind (perhaps

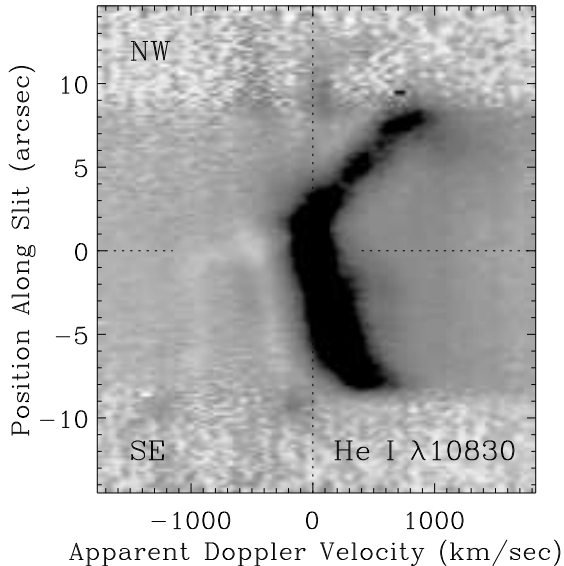


Figure 20. Same as for He I $\lambda 10830$ in Figure 17, but stretched horizontally and displayed to emphasize faint emission. Notice the blueshifted absorption in the SE lobe.

10 to 100 stellar radii; see Hillier et al. 2001) where asymmetries arise. Spatial variation in these line profiles are worth a more detailed look with higher spectral resolution.

7 SUMMARY

Spatially-resolved IR data reveal numerous details of the apparent spectrum as a function of position in the Homunculus, described above. General results are summarized here:

1. Kinematic structure of [Fe II] and H₂ lines in the Homunculus give the clearest picture yet of the geometry of the polar lobes, with $i \approx 42^\circ$. The far side of the SE lobe is seen clearly for the first time in these emission lines.

2. These near-IR spectra reveal bright [Fe II] emission from a ‘Little Homunculus’ that was discovered previously at optical wavelengths (Ishibashi et al. 2003), and offer some constraints on the physical conditions in that relatively small bipolar nebula. The Little Homunculus has no H₂ emission.

3. [Fe II] emission and He I $\lambda 10830$ absorption reveal the existence of fast moving material outside the Homunculus that is projected along the line-of-sight to the SE polar lobe.

4. The Fan and other equatorial ejecta have different spectral characteristics than the polar lobes, including blueshifted He I $\lambda 10830$ emission that apparently comes from material ejected after the Great Eruption.

5. The Weigelt blobs appear to be marginally resolved in these long-slit near-IR spectra. Subtracting the star’s spectrum allows the IR spectrum of the Weigelt blobs to be isolated for the first time.

6. There is a strong *directional dependence of excitation* in η Car’s circumstellar ejecta. IR spectra of equatorial gas are characteristic of radiative excitation and Ly α fluorescence, whereas polar ejecta are collisionally excited (either due to shocks or indirect radiative heating). In other words, ejecta near the equator “see” strong emission in the Lyman

continuum, and polar ejecta do not. This has important implications for the geometry of η Car’s UV radiation field, and that geometry seems qualitatively consistent with the stellar wind structure during η Car’s normal high-excitation state proposed by Smith et al. (2003).

7. Reflected emission in the Homunculus provides multiple viewing angles to the star, and IR wind lines show some interesting variation (although not as dramatic as Balmer absorption). Both He I $\lambda 10830$ and $\lambda 20581$ show P Cygni absorption at nearly all latitudes at roughly -550 km s^{-1} , whereas IR hydrogen lines show pure emission profiles. Other details are discussed as well. For instance, high speed He I $\lambda 10830$ absorption arises in an outer nebula, rather than in a fast component of the stellar wind.

As implied frequently in this paper, these results can be improved upon with higher spectral and spatial resolution that will soon become available. In particular, such data can give us the first look at the detailed clumpy structure of H₂ in the polar lobes and its relation to ionized gas, they can give us the best kinematic map of the Little Homunculus, and adaptive optics will hopefully allow the IR spectrum of the Weigelt blobs to be spatially-resolved without uncertainties associated with the method used in this paper. Improved spectral resolution combined with long-slit spectroscopy will also help us understand latitudinal variations in He I $\lambda 10830$ and other reflected lines. Finally, we must not forget that η Car is a notorious variable star. The directional dependence of excitation indicated by IR emission lines may respond to changes in the latitudinal density structure of η Car’s wind during its 5.5 year spectroscopic cycle (Smith et al. 2003), so emission from circumstellar gas should also be monitored with long-slit IR spectroscopy.

ACKNOWLEDGMENTS

I am grateful to Bob Blum and Patrice Bouchet for their help during the OSIRIS observing run, and to an anonymous referee for useful comments on the manuscript. Examining data obtained with *HST/STIS* has colored my interpretation of the IR spectra, and STIS measurements included in Figure 5 resulted from extant work done in collaboration with K. Davidson, T.R. Gull, K. Ishibashi, and J. Hillier. Conversations with K. Ishibashi were helpful in regard to the Little Homunculus discussed in §4, and I benefitted from discussions with G. Ferland about excitation in the Homunculus. NOAO paid for my travel to Chile and accommodations while at CTIO. I am also grateful for the support of a NASA GSRP fellowship from Goddard Space Flight Center.

REFERENCES

- Allen D.A., Jones T.J., & Hyland A.R. 1985, ApJ, 291, 280
 Allen D.A., & Hillier D.J. 1993, Proc. astron. Soc. Australia, 10, 338
 Currie D.G. et al. 1996, AJ, 112, 1115
 Currie D.G., & Dowling D.M. 1999, in ASP Conf. Ser. 179, Eta Carinae at the Millennium, ed. J.A. Morse, R.M. Humphreys, & A. Damineli (San Francisco: ASP), 72
 Damineli A. 1996, ApJ, 460, L49
 Damineli A., Stahl O., Kaufer A., Wolf B., Quast G., & Lopes D.F. 1998, A&A SS, 133, 299
 Davidson K., Ebbets D., Weigelt G., Humphreys R.M., Hajian A.R., Walborn N.R., & Rosa M. 1995, AJ, 109, 1784
 Davidson K., Ebbets D., Johansson S., Morse J.A., Hamann F.W., Balick B., Humphreys R.M., Weigelt G., & Frank A. 1997, AJ, 113, 335
 Davidson K., Smith N., Gull T.R., Ishibashi K., & Hillier D.J. 2001, AJ, 121, 1569

- Dwarkadas V.V., & Balick B. 1998, *AJ*, 116, 829
- Ferland G., Davidson K., & Smith N. 2002, in preparation
- Frank A., Balick B., & Davidson K. 1995, *ApJ*, 455, 160
- Frank A., Ryu D., & Davidson K. 1998, *ApJ*, 500, 291
- Gaviola E. 1950, *ApJ*, 11, 408
- Gehrz R.D., & Ney E.P. 1972, *S&T*, 44, 4
- Graham J.R., Wright G.S., & Longmore A.J. 1987, *ApJ*, 313, 852
- Graham J.R., Wright G.S., & Longmore A.J. 1990, *ApJ*, 352, 172
- Hamann F., Davidson K., Ishibashi K., & Gull T.R. 1999, in *ASP Conf. Ser.* 179, *Eta Carinae at the Millenium*, ed. J.A. Morse, R.M. Humphreys, & A. Damineli (San Francisco: ASP), 116
- Hamann F., DePoy D.L., Johansson S., & Elias J. 1994, *ApJ*, 422, 626
- Hartman H., Zethson T., Johansson S., Gull T., Ishibashi K., Davidson K., & Smith N. 2001, in *ASP Conf. Ser.* 242, *Eta Carinae and Other Mysterious Stars: The Hidden Opportunities of Emission Line Spectroscopy*, ed. T.R. Gull, S. Johansson, & K. Davidson (San Francisco: ASP), 107
- Hillier D.J. 1997, in *ASP Conf. Ser.* 120, *Luminous Blue Variables: Massive Stars in Transition*, ed. A. Nota & H.J.G.L.M. Lamers (San Francisco: ASP), 287
- Hillier D.J., & Allen D.A., 1992, *A&A*, 262, 153
- Hillier D.J., Davidson, K., Ishibashi, K., & Gull, T.R. 2001, *ApJ*, 553, 837
- Hofmann K.H., & Weigelt G. 1988, *A&A*, 203, L21
- Ishibashi K., et al. 2003, *AJ*, submitted
- Johansson S., & Letokhov V.S. 2001, *A&A*, 378, 266
- Johansson S., Zethson T., Hartman H., Ekberg J.O., Ishibashi K., Davidson K., & Gull T.R. 2000, *A&A*, 361, 977
- McGregor P.J., Hyland A.R., & Hillier D.J. 1988, *ApJ*, 324, 1071
- McKee C.F., Chernoff D.F., & Hollenbach D.J. 1984, in *Galactic and Extragalactic Infrared Spectroscopy*, ed. M.F. Kessler & J.P. Phillips (Dordrecht: Reidel), 103
- Meaburn J., Wolstencroft R.D., & Walsh J.R. 1987, *A&A*, 181, 333
- Meaburn J., Walsh J.R., & Wolstencroft R.D. 1993, *A&A*, 268, 283
- Moorwood A.F.M., & Oliva E. 1988, *A&A*, 203, 278
- Morse J.A., Davidson K., Bally J., Ebbets D., Balick B., & Frank A. 1998, *AJ*, 116, 2443
- Morse J.A., Kellogg J.R., Bally J., Davidson K., Balick B., & Ebbets D. 2001, *ApJ*, 548, L207
- Mouri H., Nishida M., Taniguchi Y., & Kawara K. 1990, *ApJ*, 360, 55
- Nussbaumer H., & Storey P.J. 1980, *A&A*, 89, 308
- Nussbaumer H., & Storey P.J. 1988, *A&A*, 193, 327
- Oliva E., Moorwood A.F.M., & Danziger I.J. 1990, *A&A*, 240, 453
- Ringuelet A.E. 1958, *Z. Astrophys.*, 46, 276
- Schulte-Ladbeck R.E., Pasquali A., Clampin M., Nota A., Hillier D.J., & Lupie, O.L. 1999, *AJ*, 118, 1320
- Seward F.D., Harnden F.R., Murdin P., & Clark D.H. 1983, *ApJ*, 267, 698
- Shull J.M., & Hollenbach D.H. 1978, *ApJ*, 220, 525
- Smith N. 2001, in *ASP Conf. Ser.* 242, *Eta Carinae and Other Mysterious Stars: The Hidden Opportunities of Emission Line Spectroscopy*, ed. T.R. Gull, S. Johansson, & K. Davidson (San Francisco: ASP), 81
- Smith N., & Davidson K. 2001, *ApJ*, 551, L101
- Smith N., Davidson K., Gull T.R., Ishibashi K., & Hillier D.J. 2003, *ApJ*, in press
- Smith N., & Gehrz R.D. 1998, *AJ*, 116, 823
- Smith N., & Gehrz R.D. 2000, *ApJ*, 529, L99
- Smith N., Gehrz R.D., Hinz P.M., Hoffmann W.F., Mamajek E.E., Meyer M.R., & Hora J.L. 2002, *ApJ*, 567, L77
- Smith N., Gehrz R.D., & Krautter J. 1998, *AJ*, 116, 1332
- Smith N., Gehrz R.D., & Krautter J. 1999, in *ASP Conf. Ser.* 179, *Eta Carinae at the Millenium*, ed. J.A. Morse, R.M. Humphreys, & A. Damineli (San Francisco: ASP), 31
- Sternberg A., & Dalgarno A. 1989, *ApJ*, 338, 197
- Thackeray A.D. 1951, *Observatory*, 71, 167
- Thackeray A.D. 1956a, *Observatory*, 76, 103
- Thackeray A.D. 1956b, *Observatory*, 76, 154
- Thackeray A.D. 1961, *Observatory*, 81, 99
- Viotti, R., Rossi, L., Cassatella, A., Altamore, A., & Baratta, G.B. 1989, *ApJS*, 71, 983
- Walborn N.R., & Liller M.H. 1977, *ApJ*, 211, 181
- Weigelt G., & Ebersberger J. 1986, *A&A*, 163, L5
- Weigelt G., et al. 1995, *RevMexAA Ser. Conf.*, 2, 11
- Whitelock P.A., Feast M.W., Carter B.S., Roberts G., & Glass I.S. 1983, *MNRAS*, 203, 385
- Whitney C.A. 1952, *Harvard Bull.*, No. 921, 8
- Zethson T., Johansson S., Davidson K., Humphreys R.M., Ishibashi K., & Ebbets D. 1999, *A&A*, 344, 211
- Zethson T., Gull T.R., Hartman H., Johansson S., Davidson K., & Ishibashi K. 2001, *AJ*, 122, 322